UNIVERSITY OF
BATH

Citation for published version:
Zeidler, A, Chirawatkul, P, Salmon, PS, Usuki, T, Kohara, S, Fischer, HE & Spencer Howells, W 2015, 'Structure of the network glass-former ZnCl: From the boiling point to the glass', Journal of Non-Crystalline Solids, vol. 407, pp. 235-245. https://doi.org/10.1016/j.jnoncrysol.2014.08.027

DOI:
10.1016/j.jnoncrysol.2014.08.027

Publication date:
2015

Document Version
Early version, also known as pre-print

Link to publication

University of Bath

Structure of the network glass-former ZnCl$_2$: From the boiling point to the glass

Anita Zeidler[a], Prae Chirawatkul[1a], Philip S. Salmon[2a], Takeshi Usuki[3a], Shinji Kohara[b], Henry E. Fischer[c], W. Spencer Howells[d]

[a]*Department of Physics, University of Bath, Bath BA2 7AY, UK*
[b]*Japan Synchrotron Radiation Research Institute, 1-1-1 Kouto, Sayo, Hyogo 679-5198, Japan*
[c]*Institut Laue-Langevin, 6 rue Jules Horowitz, BP 156, F-38042, Grenoble Cédex 9, France*
[d]*ISIS Facility, Rutherford Appleton Laboratory, Chilton, Didcot, Oxon OX11 0QX, UK*

Abstract

The structure of the network glass-forming material ZnCl$_2$ was measured using both neutron and high-energy x-ray diffraction for the glass at 298(1) K and for the liquid over the temperature range 601(1)–977(2) K. Intermediate range order, as manifested by the appearance of a first-sharp diffraction peak in the measured diffraction pattern for the glass at a scattering vector $k_{\mathrm{FSDP}} \simeq 1$ Å^{-1}, is retained in the liquid state even at temperatures close to the boiling point. The correlation lengths associated with both the intermediate and extended range ordering are found to be inversely proportional to temperature. The reverse Monte Carlo (RMC) method was used to model the material, and the results at two different temperatures are compared to those obtained from RMC models based on the partial structure factors measured by using the method of isotope substitution in neutron diffraction. The models show temperature dependent structural variability in which there is an interplay between the fractions of corner-sharing versus edge-sharing ZnCl$_4$ tetrahedra. Corner-sharing motifs are predominant in the glass, and edge-sharing motifs become more numerous in the liquid

[1]Present address: Synchrotron Light Research Institute (Public Organization), PO. Box 93, Nakhon Ratchasima 30000, Thailand

[2]Corresponding author: p.s.salmon@bath.ac.uk

[3]Usual address: Department of Material and Biological Chemistry, Faculty of Science, Yamagata University, 1-4-12 Koshirakawa, Yamagata 990-8560, Japan

as the temperature is increased. The appearance of a first-sharp diffraction peak in the Bhatia-Thornton concentration-concentration partial structure factor is discussed in the context of classifying the different network types for glass-forming materials.

1. Introduction

The structure of network glass-forming liquids over multiple length scales, and the evolution of this structure with temperature, is important for understanding the physical properties of these technologically important materials [1–5]. In the case of tetrahedral glass-forming systems with the MX_2 stoichiometry, the structure is described by two length scales at distances larger than the nearest-neighbor distance [6], and there is a competition between the ordering on these length scales that affects a melt's 'fragility' [7]. The length scales are associated with atomic-scale ordering on the intermediate and extended ranges, and manifest themselves in the measured diffraction patterns by the appearance of a first-sharp diffraction peak (FSDP) and a principal peak. These peaks appear at scaled positions of $k_{\mathrm{FSDP}} r_{\mathrm{MX}} \simeq 2.5$ and $k_{\mathrm{PP}} r_{\mathrm{MX}} \simeq 4.8$ where k_{FSDP} and k_{PP} are the scattering vectors for the FSDP and principal peak, respectively, and r_{MX} is the nearest-neighbor distance for unlike chemical species [8–12]. The competition between the ordering on these length scales manifests itself in terms of the relative importance of the FSDP versus the principal peak in the Bhatia-Thornton [13] number-number partial structure factor $S_{NN}^{\mathrm{BT}}(k)$ which describes the topological ordering. The FSDP in $S_{NN}^{\mathrm{BT}}(k)$ is more prominent than the principal peak for 'strong' glass formers such as GeO_2, whilst the converse holds true for more 'fragile' glass formers such as $ZnCl_2$ and $GeSe_2$ [7, 12, 14]. The 'strong' versus 'fragile' taxonomy for glass-forming liquids originates from the temperature dependence of the viscosity near the glass transition temperature T_g [15]. Fragile materials show a particularly rapid increase of viscosity near T_g which affects their manipulability e.g. it may be necessary to supercool a fragile liquid in order for its viscosity to become sufficiently large to enable fiber-pulling [16].

In this paper we explore the evolution with temperature of the atomic scale ordering in the glass-forming system $ZnCl_2$ [6, 17–34] by using a combination of neutron and high energy x-ray diffraction to investigate the glass

2

at 298(1) K and the liquid at several temperatures in the range 601(1)–977(2) K i.e. close to the melting and boiling points at 563 and 1005 K, respectively [35]. This material is a prototypical example of a glass-former with structure-related properties that can be understood in terms of an ionic interaction model, provided that anion polarization effects are taken into account [23, 27, 29–31]. The basic structure of the glass can be thought of in terms of a random close-packed distribution of Cl atoms where the Zn atoms occupy tetrahedral holes and are arranged in a way that maximizes the number of corner-sharing $ZnCl_4$ tetrahedra [21]. The structure can also be thought of in terms of a network of corner-sharing $ZnCl_4$ tetrahedra in which the Cl atoms are densely packed. For example, molecular dynamics simulations on MX_2 systems show that a SiO_2-like structure can be transformed to a $ZnCl_2$-like structure via a systematic increase of the anion polarizability [36, 37]. Thus, $ZnCl_2$ can also be regarded as a network glass-former albeit with a topology that is different to materials such as SiO_2 e.g. at ambient pressure the coordination number of the electronegative species can vary from two (Section 5.1). The fragility of liquid $ZnCl_2$ is intermediate between strong glass-forming systems such as SiO_2 and GeO_2 and more fragile glass forming systems such as $KCl–BiCl_3$ and $Ca_2K_3(NO_3)_7$ [15, 24, 38, 39].

Part of the motivation for the present study is a search in glass-forming systems for a growing static length scale which should accompany a slow down in the dynamics as the glass transition is approached i.e. the time taken for a system to relax increases because correlated regions of growing size need to rearrange [40]. The alterations to the measured structure factors for glass-forming liquids as T_g is approached are, however, small as compared to dynamical properties such as the viscosity and diffusion coefficients which change by many orders of magnitude [41, 42]. Nevertheless, it is of value to measure the temperature dependent structural changes in $ZnCl_2$ because this system is ionic and is therefore amenable to investigation by molecular dynamics methods using a polarizable ion model [23, 27, 29, 30, 37, 43]. Such methods allow for access to several of the pertinent length and time-scales e.g. the extended range ordering in tetrahedral MX_2 glasses can persist to nanometer length-scales of 20–30 Å [6, 7, 12, 44, 45].

The diffraction data were modeled by using the reverse Monte Carlo (RMC) method [46], and the full set of partial structure factors were extracted for several temperatures, together with the associated bond angle distributions and ring statistics. We find that the network structure of the glass is made predominantly from corner-sharing $ZnCl_4$ tetrahedra, although

3

there are also edge-sharing tetrahedra which become more numerous in the liquid with increasing temperature. The structural motifs organize on an intermediate length scale to give an FSDP in the measured diffraction patterns at $k_{\mathrm{FSDP}} \simeq 1$ Å^{-1} which remains a significant feature of the liquid state even at temperatures close to the boiling point. The appearance of edge-sharing motifs is consistent with molecular dynamics work on tetrahedral glass-forming MX_2 systems which suggests that by disrupting networks of corner-sharing tetrahedra they promote melts with increased fragility [36].

The manuscript is organized as follows. In Section 2, the essential theory is described for understanding the diffraction results. In Section 3, an outline is given of the sample preparation and characterization methods, the neutron and x-ray diffraction experiments, and the RMC procedure used to model the structure. The resolution function correction applied to the neutron diffraction data is also described. Next, in Section 4, the neutron and x-ray diffraction results for the glass and liquid are presented, and the results obtained from the RMC models are compared to those obtained from previous RMC work in which the full set of partial structure factors were measured by using neutron diffraction with isotope substitution (NDIS) for the glass at 298(1) K and for the liquid at 605(5) K [32]. In Section 5, the results are discussed in terms of the temperature dependence of the structural motifs, bond angle distributions and ring statistics, and also in terms of the Bhatia-Thornton [13] partial structure factors which separate the topological from the chemical ordering. Finally, in Section 6 the conclusions are summarized.

2. Theory

In a neutron or x-ray diffraction experiment on glassy or liquid $ZnCl_2$ the total structure factor [47]

$$F(k) = \sum_\alpha \sum_\beta c_\alpha c_\beta f_\alpha(k) f_\beta^*(k) \left[S_{\alpha\beta}(k) - 1 \right] \tag{1}$$

is measured, where α and β denote the chemical species, c_α represents the atomic fraction of chemical species α, $f_\alpha(k)$ and $f_\alpha^*(k)$ are the form factor (or scattering length) for chemical species α and its complex conjugate, respectively, $S_{\alpha\beta}(k)$ is a Faber-Ziman [48] partial structure factor, and k is the magnitude of the scattering vector. $S_{\alpha\beta}(k)$ is related to the partial pair-

4

distribution function $g_{\alpha\beta}(r)$ via the Fourier transform

$$g_{\alpha\beta}(r) - 1 = \frac{1}{2\pi^2\,\rho\,r} \int_0^\infty dk\,k\,[S_{\alpha\beta}(k) - 1]\,\sin(kr) \qquad (2)$$

where ρ is the atomic number density and r is a distance in real space. The mean coordination number of atoms of type β, contained in a volume defined by two concentric spheres of radii r_i and r_j centered on an atom of type α, is given by

$$\bar{n}_\alpha^\beta = 4\pi\,\rho\,c_\beta \int_{r_i}^{r_j} dr\,r^2 g_{\alpha\beta}(r). \qquad (3)$$

The scattering lengths in neutron diffraction are independent of k but the form factors in x-ray diffraction are k-dependent. In order to compensate for this k-dependence, the total structure factor is often rewritten as

$$S(k) - 1 = \frac{F(k)}{|\langle f(k)\rangle|^2} \qquad (4)$$

where $\langle f(k)\rangle = c_{Zn}f_{Zn}(k) + c_{Cl}f_{Cl}(k)$ is the mean form factor. The corresponding real-space information is provided by the total pair-distribution function as obtained from the Fourier transform

$$G(r) - 1 = \frac{1}{2\pi^2\,\rho\,r} \int_0^\infty dk\,k\,[S(k) - 1]\,\sin(kr). \qquad (5)$$

In the case of x-ray diffraction experiments, the normalization defined by Eq. (4) has the advantage that it allows for a better resolution of the peaks in $G(r)$. For r values smaller than the distance of closest approach between the centers of two atoms $g_{\alpha\beta}(r) = g_{\alpha\beta}(r \to 0) = 0$ such that $G(r) = G(r \to 0) = 0$.

The total structure factor can also be written in terms of the Bhatia-Thornton [13] number-number, concentration-concentration and number-concentration partial structure factors denoted by $S_{NN}^{BT}(k)$, $S_{CC}^{BT}(k)$ and $S_{NC}^{BT}(k)$, respectively, where

$$\begin{aligned}
F(k) &= |\langle f(k)\rangle|^2 S_{NN}^{BT}(k) + |f_{Zn}(k) - f_{Cl}(k)|^2 S_{CC}^{BT}(k) \\
&+ \{\langle f(k)\rangle\,[f_{Zn}(k)^* - f_{Cl}(k)^*] + \langle f(k)\rangle^*\,[f_{Zn}(k) - f_{Cl}(k)]\}\,S_{NC}^{BT}(k) \\
&- \left[c_{Zn}|f_{Zn}(k)|^2 + c_{Cl}|f_{Cl}(k)|^2\right].
\end{aligned} \qquad (6)$$

5

The $S_{IJ}^{\mathrm{BT}}(k)$ ($I, J = N, C$) and $S_{\alpha\beta}(k)$ ($\alpha, \beta = \mathrm{Zn, Cl}$) partial structure factors are related by the equations

$$S_{NN}^{\mathrm{BT}}(k) = c_{\mathrm{Zn}}^2 S_{\mathrm{ZnZn}}(k) + c_{\mathrm{Cl}}^2 S_{\mathrm{ClCl}}(k) + 2c_{\mathrm{Zn}}c_{\mathrm{Cl}}S_{\mathrm{ZnCl}}(k), \tag{7}$$

$$S_{CC}^{\mathrm{BT}}(k) = c_{\mathrm{Zn}}c_{\mathrm{Cl}}\left\{1 + c_{\mathrm{Zn}}c_{\mathrm{Cl}}\left[S_{\mathrm{ZnZn}}(k) + S_{\mathrm{ClCl}}(k) - 2S_{\mathrm{ZnCl}}(k)\right]\right\}, \tag{8}$$

$$S_{NC}^{\mathrm{BT}}(k) = c_{\mathrm{Zn}}c_{\mathrm{Cl}}\left\{c_{\mathrm{Zn}}\left[S_{\mathrm{ZnZn}}(k) - S_{\mathrm{ZnCl}}(k)\right] - c_{\mathrm{Cl}}\left[S_{\mathrm{ClCl}}(k) - S_{\mathrm{ZnCl}}(k)\right]\right\} \tag{9}$$

It follows from Eq. (6) that in a diffraction experiment $S_{NN}^{\mathrm{BT}}(k)$ would be measured directly if $f_{\mathrm{Cl}}(k) = f_{\mathrm{Zn}}(k)$ (which could be achieved in a neutron diffraction experiment by a suitable choice of Cl isotopes), whereas $S_{CC}^{\mathrm{BT}}(k)$ would be measured directly if $\langle f(k) \rangle = 0$. The Fourier transform of $S_{NN}^{\mathrm{BT}}(k)$, denoted by $g_{NN}^{\mathrm{BT}}(r)$, describes the pair-correlations between the sites of the scattering centers but cannot distinguish between the chemical species that occupy those sites i.e. it gives information on the topological ordering. In comparison, the Fourier transform of $S_{CC}^{\mathrm{BT}}(k)$, denoted by $g_{CC}^{\mathrm{BT}}(r)$, gives information on the chemical ordering i.e. on the occupancy by Zn and Cl atoms of the sites described by $g_{NN}^{\mathrm{BT}}(r)$. A preference for like or unlike neighbors at a given distance will lead to a corresponding positive or negative peak in $g_{CC}^{\mathrm{BT}}(r)$, respectively. The Fourier transform of $S_{NC}^{\mathrm{BT}}(k)$, denoted by $g_{NC}^{\mathrm{BT}}(r)$, describes the cross-correlation between the sites of the scattering centers and their occupancy by a given chemical species. A more complete description of the Bhatia-Thornton formalism as applied to MX_2 systems is given elsewhere [12, 49].

In the following, the notation $S_{\mathrm{N}}(k)$ and $S_{\mathrm{X}}(k)$ will be used in order to distinguish between the total structure factors measured by neutron and x-ray diffraction and the corresponding total pair-distribution functions will be denoted by $G_{\mathrm{N}}(r)$ and $G_{\mathrm{X}}(r)$, respectively. The coherent neutron scattering lengths for Zn and Cl of natural isotopic abundance are 5.680(5) and 9.5770(8) fm, respectively [50]. The weighting factors for the Zn–Zn, Zn–Cl and Cl–Cl partial structure factors are 0.0523:0.3528:0.5949 for $S_{\mathrm{N}}(k)$ versus 0.1914:0.4922:0.3164 for $S_{\mathrm{X}}(k)$ at $k = 0$ if Zn^{2+} and Cl^- ions are assumed i.e. neutron diffraction gives complementary information to x-ray diffraction. The assumption of full formal charges for zinc and chlorine is supported by an ability to reproduce the main structural features of liquid ZnCl_2 by using a polarizable ion model with these charges [23, 27, 29, 30].

3. Experimental and modeling procedures

3.1. Sample preparation

For the neutron diffraction experiment, anhydrous beads of $ZnCl_2$ (99.999%, Sigma-Aldrich) with the natural isotopic abundance were loaded into a cylindrical silica ampoule of 4 mm inner diameter and 1 mm wall thickness within a high-purity argon-filled glove-box. The ampoule was then sealed under a vacuum of $\approx 10^{-5}$ torr. The glass transition temperature T_g of the beads was measured to be 376(2) K (mid-point) from the reversible part of the heat flow measured using a TA Instruments Q100 modulated differential scanning calorimeter with a scan rate of 3 K min^{-1}, modulation of ± 1 K per 60 s and an oxygen-free nitrogen gas flow rate of 25 ml min^{-1}. These results compare with literature T_g values of 376–380 K [51], 370 K [52] and 375(5) K [53].

For the x-ray diffraction experiment, anhydrous beads of $ZnCl_2$ were loaded into a silica container connected to a cylindrical silica capillary tube of 1.8 mm inner diameter and 0.6 mm wall thickness. The apparatus was sealed under a vacuum of $\approx 10^{-5}$ torr and placed in an oven at 1073 K with the tip of the capillary tube located outside of the oven door. $ZnCl_2$ vapor was allowed to condense into this cooler part of the apparatus and the capillary tube was then sealed under high vacuum. The sample was vitrified by heating the capillary tube to ≈ 723 K and quenching in an ice-water mixture.

3.2. Diffraction experiments

The neutron diffraction experiment was performed using the instrument D4c [54] at the Institut Laue-Langevin (ILL) with an incident wavelength of 0.4967(1) Å. A vanadium furnace was used in which a cylindrical heating element of 17 mm diameter and 0.1 mm wall thickness was surrounded by a cylindrical heat shield of 25 mm diameter and 0.04 mm wall thickness. Diffraction patterns were measured at 708(2), 808(2), 906(2) and 977(2) K for the sample in its container in the furnace, for an empty container in the furnace, and for the empty furnace. Diffraction patterns were also measured at room temperature for the empty furnace; for a cylindrical vanadium rod of diameter 6.37(1) mm in the furnace; and for a bar of neutron absorbing $^{10}B_4C$ of dimensions comparable to the sample in the furnace. The vanadium data were used for normalization purposes and the $^{10}B_4C$ data were used to help in accounting for the effect of sample attenuation on the background signal at small scattering angles [55]. The stability of the sample and instrument at each temperature was assessed by saving the measured diffraction

patterns at regular intervals [56]. For the sample measurements at each of the temperatures 708(2), 808(2) and 906(2) K no deviation between the finally selected patterns was observed within the counting statistics. For the sample measurement at a temperature of 977(2) K, however, deviations resulted from the formation of bubbles in the liquid. Patterns were therefore selected to give a composite diffraction pattern in which the effect of these deviations canceled to first order. Neutron diffraction experiments on the glass at 298(1) K and on the liquid at 605(5) K were also performed using the D4c instrument with an incident wavelength of $\simeq 0.5$ Å and are described elsewhere [6, 32].

The measured $S_N(k)$ functions were extrapolated in the range $0 \le k \lesssim 0.5$ Å^{-1} to the $S_N(k \to 0)$ limit by assuming that $S_N(k) \propto k^2$ [44, 45]. For the liquid, the limiting values were calculated from Eqs. (4) and (6) by assuming an ionic interaction model for ZnCl$_2$ in which $S_{CC}^{\mathrm{BT}}(k \to 0) = S_{NC}^{\mathrm{BT}}(k \to 0) = 0$ and $S_{NN}^{\mathrm{BT}}(k \to 0) = \rho k_B T \kappa_T$ where k_B is the Boltzmann constant, T is the absolute temperature and κ_T is the isothermal compressibility [44, 45]. Values for the latter (see Table 1) were obtained by using $\kappa_T = \gamma \kappa_S$ where $\gamma = C_p/C_v$ is the ratio of the constant pressure to constant volume heat capacities. For the liquid $\gamma = 1.04$ at temperatures of 400, 500 and 600 °C and $\gamma = 1.05$ at 700 °C [57]. Sound velocity measurements show that the adiabatic compressibility over the temperature range 410–705 °C is given by [57]

$$\kappa_s = a + bt + ct^2 \tag{10}$$

where the coefficients take values of $a = 33.2 \times 10^{-11}$ Pa^{-1}, $b = 1.30 \times 10^{-13}$ Pa^{-1} °C^{-1} and $c = 3.701 \times 10^{-16}$ Pa^{-1} °C^{-2}, t is the temperature in Celsius, and the error on κ_s is $\pm 1\%$. At lower temperatures, κ_s takes values of 3.63×10^{-10}, 3.85×10^{-10}, 3.99×10^{-10} and 4.19×10^{-10} Pa^{-1} at 319, 329, 342.5 and 365.9 °C, respectively.

The high-energy x-ray diffraction experiments were performed using beamline BL04B2 at SPring-8 [58]. The (220) planes of a silicon monochromator were used to give an incident x-ray wavelength of 0.20095(5) Å (energy $\simeq$ 61.7 keV), and the incident beam intensity was monitored by an ionization chamber filled with Ar gas of 99.99% purity. The samples were held in a vacuum bell jar to avoid air scattering, and the diffracted x-rays were collected using a Ge solid-state detector. Diffraction patterns were measured at room temperature for the glass in its container and for an empty container. Diffraction patterns were also measured at temperatures of 601(1), 613(1),

Table 1: The temperature T dependence of the atomic number density ρ and isothermal compressibility κ_T for glassy and liquid $ZnCl_2$ together with the first two peak positions r_1 and r_2 in the $G_N(r)$ or $G_X(r)$ functions measured by either neutron diffraction (ND) or x-ray diffraction (XRD), and the mean Zn–Cl coordination number $\bar{n}_{Zn}^{Cl}$. The packing fraction of Cl atoms η_{Cl} at selected temperatures is also given.

T (K)	ρ (Å^{-3})	κ_T (10^{-10} Pa^{-1})	r_1 (Å)	r_2 (Å)	$\bar{n}_{Zn}^{Cl}$	η_{Cl}	Method
298(1)	0.0359(1)	–	2.28(2)	3.70(2)	4.00(8)	0.647	ND[a]
		–	2.27(2)	3.71(2)	4.04(5)		XRD
601(1)	0.0334(1)	4.00(4)	2.27(2)	3.73(2)	3.93(5)	0.594	XRD
603(1)	0.0334	–	2.28(1)	3.79(2)[b]	3.93(6)		ND[c]
605(5)	0.0334(1)	4.03(4)	2.27(2)	3.72(2)	4.12(5)		ND[d]
613(1)	0.0333(1)	4.15(4)	2.27(2)	3.72(2)	3.94(5)		XRD
703(1)	0.0327(1)	4.75(5)	2.27(2)	3.76(3)	3.90(5)	0.581	XRD
708(2)	0.0326(1)	4.77(5)	2.28(2)	3.71(2)	4.01(5)		ND
803(1)	0.0320(1)	5.25(5)	2.27(2)	3.83(5)	3.87(5)	0.569	XRD
808(2)	0.0320(1)	5.28(5)	2.27(2)	3.72(2)	4.01(5)		ND
873(1)	0.0318	–	2.29(1)	3.86(5)[b]	3.67(7)		ND[c]
903(1)	0.0315(1)	5.83(6)	2.27(2)	3.75(3)	3.85(5)	0.560	XRD
906(2)	0.0314(1)	5.85(6)	2.28(2)	3.70(2)	3.96(10)		ND
977(2)	0.0311(1)	6.37(6)	2.27(2)	3.66(2)	3.91(6)	0.553	ND

[a] Data taken from Refs. [6, 32]; [b] peak position in $r^2 G_N(r)$; [c] data taken from Ref. [22]; [d] data taken from Ref. [32].

703(1), 803(1) and 903(1) K for the liquid in its container in the furnace, and for an empty container in the furnace. The data analysis procedure, which is described elsewhere [58], used ionic form factors for Zn^{2+} and Cl^- [59], and Compton scattering corrections taken from Refs. [60, 61].

The mass density $\rho_{mass}(T)$ of the liquid at absolute temperature T was calculated from the expression [62]

$$\rho_{mass}(T) = a' + b'T + c'T^2 \tag{11}$$

where the coefficients take values of $a' = 3.0183$ g cm^{-3}, $b' = -1.0536 \times 10^{-3}$ g cm^{-3} K^{-1} and $c' = 3.7641 \times 10^{-7}$ g cm^{-3} K^{-2}. The corresponding number densities are listed in Table 1.

3.3. Resolution function correction

The neutron diffraction data were corrected to yield the total structure factor for each sample [63, 64]. Previous work on liquid and glassy $ZnCl_2$ using the NDIS method has, however, shown that it is necessary to apply a resolution function correction to the neutron diffraction results if they are to be consistent with the x-ray diffraction results, particularly in the region of the FSDP [32]. Essentially, the resolution function for the neutron diffractometer D4c is broader than for the x-ray diffractometer on beamline BL04B2 and it is asymmetric at smaller k-values owing to the so-called umbrella effect [65–67]. In the present work, a correction for the resolution function of the diffractometer was therefore applied to the neutron diffraction patterns for the glass and liquid by using the moments method of deconvolution [67, 68]. The resolution function correction for the x-ray diffractometer was found to be negligible in comparison with the neutron diffractometer, and a correction for the x-ray data was not therefore made.

3.4. Reverse Monte Carlo (RMC) modeling

The program RMC++ [69] was used to obtain atomistic models for glassy and liquid $ZnCl_2$. The $S_X(k)$ and resolution-function corrected $S_N(k)$ functions were used to constrain the model for the glass and for the liquid at average temperatures of 603(5), 706(3), 806(3) and 905(2) K, and only the resolution-function corrected $S_N(k)$ function was used to constrain the model for the liquid at 977(2) K. Each model contained 3000 atoms in a cubic box of side length chosen to give the correct atomic number density (Table 1). The starting configurations for the glass and for the liquid at different temperatures were taken from RMC models based on previous NDIS experiments in which the full set of partial structure factors were measured for the glass and for the liquid at 605(5) K [32]. Coordination number constraints were not applied, and use was made of nearest-neighbor Zn–Cl, Zn–Zn, Cl–Cl cut-off distances of 2.1, 3.4, 3.2 Å for the glass, and 2.0–2.1, 2.8–2.9, 2.9 Å for the liquid, respectively. The RMC results for the liquid at 977 K are likely to be the least reliable since, in the absence of x-ray diffraction data, only $S_N(k)$ could be used to constrain the model.

4. Results

The measured $S_N(k)$ functions before and after the resolution function correction are compared in Fig. 1, and show that the main effect of this

correction occurs in the region of the FSDP. The measured $S_X(k)$ functions are illustrated in Fig. 2. The first three peak positions k^* in the total structure factors are given in Fig. 3 and show a weak temperature dependence. The corresponding correlation lengths, as estimated by the expression $2\pi/\Delta k^*$ where Δk^* is a peak full-width at half-maximum [10], are given in Fig. 4. The larger spread of values associated with the FSDP in $S_N(k)$ is probably related to the small size of this feature. The results show that the correlation lengths are inversely proportional to temperature.

The total pair-correlation functions $G_N(r)$ and $G_X(r)$ are illustrated in Figs. 5 and 6, respectively. The first peak in both functions is attributed to nearest-neighbor Zn–Cl correlations [6, 19, 32], such that the broadening of this feature with increasing temperature amounts to a broadening of the first peak in $g_{ZnCl}(r)$. The coordination number $\bar{n}_{Zn}^{Cl}$ was extracted by integrating over this first peak in $g_{ZnCl}(r)$ after extrapolating the large-r side of the peak to the $g_{ZnCl}(r \rightarrow 0)$ limit. In the case of the x-ray diffraction data, the r-space effect of the k-dependent form factors was removed by adopting the procedure described in Ref. [70]. The results show no substantial change in either the Zn–Cl bond distances or coordination numbers with increasing temperature (Table 1).

The RMC fits to the $S_N(k)$ and $S_X(k)$ functions are shown in Figs. 1–2, and the corresponding Faber-Ziman partial structure factors $S_{\alpha\beta}(k)$ are shown in Fig. 7. The largest FSDP occurs for $S_{ZnZn}(k)$, in agreement with the findings from experiments using the NDIS method [6, 19, 32], but in disagreement with other work in which neutron and x-ray diffraction results were combined [26]. The features in the $S_{\alpha\beta}(k)$ functions for the glass dampen with increasing temperature but there is otherwise little change e.g. the FSDP in $S_{ZnZn}(k)$ remains even at the highest temperature. There are, however, differences in detail in the region of the FSDP between the $S_{\alpha\beta}(k)$ functions from the present work and those obtained for the glass and for the liquid at 605(5) K by using the NDIS method [32]. For example, the FSDP in $S_{ZnZn}(k)$ from the present work is sharper and less asymmetric (Section 3.3). These changes are consistent with the effect of constructing partial structure factors either before [32] or after (present work) a resolution function correction is made to the neutron diffraction data. In the work of Zeidler *et al.* [32] it was shown that, if the x-ray total structure factor reconstructed from the NDIS results $S_X^{rec}(k)$ is to be matched in the FSDP region with the measured x-ray total structure factor $S_X^{meas}(k)$, then a resolution function correction needs to be made to $S_X^{rec}(k)$.

The RMC partial pair-distribution functions $g_{\alpha\beta}(r)$ are shown in Fig. 8. In the case of $g_{\mathrm{ZnZn}}(r)$, the first peak appears at $\simeq 3.74$ Å for the glass [6, 32] and arises predominantly from corner-sharing $\mathrm{ZnCl_4}$ tetrahedra. In the liquid phase, this peak develops a small-r tail that is consistent with the appearance of edge-sharing tetrahedra, where typical Zn–Zn distances are 3.16–3.24 Å [71]. The first peak in the other $g_{\alpha\beta}(r)$ functions also broadens with increasing temperature. Further analysis is required to reveal the accompanying structural changes (Section 5).

5. Discussion

5.1. Temperature dependent structure of ZnCl$_2$

The distribution in the number of α-fold coordinated zinc atoms Znα (α = 2, 3, 4, 5 or 6) and α-fold coordinated chlorine atoms Clα (α = 1, 2, 3 or 4) at each temperature was found from the RMC configurations by using the bond properties code within the Interactive Structure Analysis of Amorphous and Crystalline Systems (ISAACS) package [72]. A Zn–Cl cut-off distance was set at 2.8 Å. The system was found to be chemically ordered at all temperatures such that Znα corresponds to ZnCl$_\alpha$ units and Clα corresponds to ClZn$_\alpha$ units. The temperature dependence of the fractions of Znα and Clα species is shown in Figs. 9(a)–(b) where a comparison is also made with the fractions obtained from the NDIS-based RMC models for the glass and for the liquid at 605(5) K [32]. The mean Zn and Cl coordination numbers at all temperatures are $\bar{n}_{\mathrm{Zn}}^{\mathrm{Cl}} \simeq 4.0$ and $\bar{n}_{\mathrm{Cl}}^{\mathrm{Zn}} \simeq 2.0$. It is found that Zn4 species dominate over the entire temperature range, although they become less numerous with increasing temperature as they are replaced by Zn3 and Zn5 species. In comparison, Cl2 species are in the majority over the entire temperature range, but there are also substantial fractions of Cl1 and Cl3 species, each at the $\simeq 20\%$ level. This observation is not expected on the basis of networks formed by corner-sharing $\mathrm{ZnCl_4}$ tetrahedra where the Cl atoms are two-fold coordinated as in the crystalline phases of ZnCl$_2$ [73–75], which points to an increased structural variability in the glass and liquid i.e. there are species other than Zn4 and Cl2. In a polarizable ion model of liquid ZnCl$_2$, the fractions of Cl1, Cl2 and Cl3 species are 11, 81 and 8% at 800 K, and 14, 78 and 8% at 1000 K, respectively [30].

The bond angle distributions shown in Fig. 10 were obtained by using additional Zn–Zn and Cl–Cl cut-off distances of 4.3 Å and 5.0 Å for the glass and 4.5 Å and 5.2 Å for the liquids, respectively. Each of these bond

12

angle distributions $B(\theta)$ is proportional to the number of bonds between θ and $\theta + \Delta\theta$ which is dependent on the solid angle $\Delta\Omega \propto \sin(\theta)$ subtended at that value of θ. The bond angle distributions are therefore plotted as $B(\theta)/\sin(\theta)$ in order to compensate for the effect of $\Delta\Omega$ such that a finite bond angle distribution at e.g. $\theta \simeq 180°$ is not artificially suppressed [32, 76]. The bond angle distributions for the glass and for the liquid at 603 K are comparable to those obtained from NDIS-based RMC models [32], with the notable exception of the Zn–Cl–Zn bond angle distribution where the NDIS-based models show a more pronounced shoulder at $\simeq 90°$. This feature corresponds to edge-sharing conformations, and there is an accompanying shoulder at $\simeq 90°$ in the Cl–Zn–Cl bond angle distribution. As shown in Fig. 9(c), the fraction of edge-sharing Zn4 species is larger in the NDIS-based RMC models [32] than in the present work. Fig. 9(c) also shows that the fraction of Zn4 species in edge-sharing versus corner-sharing tetrahedra is temperature dependent, with the fraction of edge-sharing motifs increasing with temperature as suggested by the increased intensity of the shoulder at $\simeq 90°$ in the Zn–Cl–Zn bond angle distribution. The observation of both edge-sharing and corner-sharing tetrahedra in glassy and molten $ZnCl_2$, and the increase with temperature in the fraction of edge-sharing tetrahedra in the liquid phase, is supported by Raman spectroscopy experiments [28]. The vapor phase of this material contains predominantly $ZnCl_2$ monomers with a small fraction of Zn_2Cl_4 dimers with D_{2h} symmetry in which the Zn atoms are bridged by two Cl atoms [71, 77–79].

The packing fraction of Cl atoms η_{Cl} for glassy and liquid $ZnCl_2$ can be estimated from the Cl atom number density $\rho_{Cl} = 2\rho/3$ by assuming hard spheres of radius r_{Cl} such that $\eta_{Cl} = (8/9)\rho\pi r_{Cl}^3$. If the Cl atoms are also touching in regular $ZnCl_4$ tetrahedra then the Cl–Cl distance $r_{ClCl} = 2r_{Cl}$ and $r_{ClCl} = \sqrt{8/3}\, r_{ZnCl}$ such that the packing fraction can be re-written as $\eta_{Cl} = 16\sqrt{2/3}\pi\rho r_{ZnCl}^3/27 = 1.520\rho r_{ZnCl}^3$ where r_{ZnCl} is the measured Zn–Cl bond length. The η_{Cl} values calculated in this way are listed in Table 1 and show a packing fraction for the glass that is comparable to the value $\simeq 0.64$ expected for a dense random packing of hard spheres [80]. Indeed, the structure of vitreous $ZnCl_2$ has been described in terms of a distorted random close-packed array of Cl atoms where the Zn atoms occupy tetrahedral holes and are arranged in a way that maximizes the number of corner sharing $ZnCl_4$ tetrahedra [21]. However, the RMC models from the present work and Ref. [32], and the Raman spectroscopy experiments from Ref. [28], point to

a glass structure that is more complicated with the presence of edge-sharing conformations. In the case of the liquid, η_{Cl} decreases by $\sim 7\%$ over the entire temperature range and the Cl–Cl–Cl bond angle distribution, which has many of the features expected for a random close-packing of Cl atoms [32], shows little change.

The ring statistics were calculated by using the Rigorous Investigation of Networks Generated using Simulation (RINGS) code [81, 82] within the ISAACS package [72]. Zn atoms were used as starting points to initiate shortest path searches using King's criterion [83] for rings containing a maximum of $n = 30$ atoms. Homopolar bonds were not excluded from the search procedure but none were found, which accounts for an absence of rings with odd n-values. A Zn–Cl cut-off distance was set at 2.8 Å, and the results are shown in Fig. 11. $R_C(n)$ is the number of rings containing n atoms (Zn or Cl), normalized to the total number of Zn atoms; $P_N(n)$ is the number of Zn atoms that can be used as a starting point to initiate a search for at least one ring containing n atoms, normalized to the total number of Zn atoms;[4] and for a given Zn atom in an n-fold ring, $P_{min}(n)$ ($P_{max}(n)$) gives the probability that this ring constitutes the shortest (longest) closed path that can be found by using this Zn atom to initiate a search.

Let's first consider the connectivity profiles shown in Fig. 11 for the glass and for the liquid at 603 K. The profile of $R_C(n)$ indicates a distribution of ring sizes that is broader for the liquid than for the glass with a minimum ring size of $n = 4$, corresponding to edge-sharing motifs, and with peaks at $n = 6$ and $n = 14$. The profile of $P_N(n)$ shows that Zn atoms can often be used as the origin of search for finding six-fold rings i.e. these rings are a significant feature of both the glass and liquid networks. The value $P_{min}(n) = 1$ for $n = 4$ means that Zn atoms within four-fold rings cannot be used as the origin of search for smaller rings i.e. edge-sharing motifs form the shortest closed paths. The value $P_{max}(n) \simeq 0.006$ for $n = 4$ implies a $\simeq 99.4\%$ chance that a Zn atom within a four-fold ring can also be used as the origin of search for a ring with $n > 4$, i.e. Zn atoms act as 'network forming' nodes [81, 82]. The connectivity profiles are similar to those obtained from the NDIS-based

---

[4]In general, $P_N(n) \neq R_N(n)$ where $R_N(n)$ is the number of atoms in an n-fold ring normalized to the total number of Zn atoms. This inequality follows because a Zn atom in a particular ring cannot necessarily be used as the origin of search for finding that ring via a shortest path algorithm [81, 82]. In the case of $ZnCl_2$, however, the network is chemically ordered and it will be assumed that $P_N(n) = R_N(n)$ for $n = 4$.

RMC models for the glass and liquid at 605 K [32], except that in the case of the NDIS-based model for the liquid the second peak in $R_C(n)$ occurs at $n = 18$ instead of $n = 14$.

At elevated temperatures, the peak in $R_C(n)$ at $n = 6$ disappears and the value of $R_C(n)$ at $n = 4$ increases as edge-sharing motifs become more numerous. The corresponding increase in value of $P_N(n)$ at $n = 4$ and decrease in value of $P_N(n)$ at $n = 6$ indicate that $n = 4$ rings become more significant network features than $n = 6$ rings with increasing temperature. The peak in $R_C(n)$ at $n = 14$ also shifts to higher n values, which is correlated with a decrease in the fraction of Zn4 species and an increase in the fraction of edge-sharing conformations (Figs. 9(a),(c)). The break-down with increasing temperature of the predominantly corner-sharing network of the glass is therefore accompanied by the appearance of larger rings, although the small $P_N(n)$ values for larger ring sizes do not suggest that these larger rings become significant network features.

When investigating MX_2 network structures containing edge-sharing conformations it is helpful to distinguish between M atoms that are involved in one edge-sharing motif $M^{(1)}$, two edge-sharing motifs $M^{(2)}$, or in no edge-sharing motifs $M^{(0)}$ [29, 31, 84]. If the motifs are tetrahedral, then an increase in the fraction of $M^{(2)}$ implies the formation of chains of edge-sharing tetrahedra as indicated by Fig. 12. To estimate the fractions of $Zn^{(i)}$ ($i = 0, 1, 2$) species in $ZnCl_2$, let's consider a chemically ordered network where $N_{Zn^{(i)}}$ is the number of $Zn^{(i)}$ species and N_{Zn} is the total number of Zn atoms such that $N_{Zn} = N_{Zn^{(0)}} + N_{Zn^{(1)}} + N_{Zn^{(2)}}$. Then the total number of Zn atoms involved in four-fold rings is given by

$$N_{Zn} P_N(n = 4) = N_{Zn^{(1)}} + N_{Zn^{(2)}}, \tag{12}$$

where $P_N(n = 4)$ is obtained by using Zn atoms to initiate a search, and it follows that

$$N_{Zn^{(0)}} = N_{Zn} - N_{Zn} P_N(n = 4). \tag{13}$$

Based on edge-sharing conformations of the type shown in Fig. 12 an 'isolated' four-fold ring will contain two $Zn^{(1)}$ atoms, and each $Zn^{(2)}$ atom will be common to two four-fold rings. The total number of four-fold rings is therefore given by

$$N_{Zn} R_C(n = 4) = \left[N_{Zn^{(1)}} + 2N_{Zn^{(2)}} \right] / 2 \tag{14}$$

where $R_C(n = 4)$ is obtained by using Zn atoms to initiate a search. It follows from Eqs. (12) and (14) that

$$N_{\mathrm{Zn}^{(2)}} = 2N_{\mathrm{Zn}}R_C(n = 4) - N_{\mathrm{Zn}}P_N(n = 4) \tag{15}$$

such that $N_{\mathrm{Zn}^{(1)}}$ can be evaluated from Eqs. (13) and (15) by using the equation

$$N_{\mathrm{Zn}^{(1)}} = N_{\mathrm{Zn}} - N_{\mathrm{Zn}^{(0)}} - N_{\mathrm{Zn}^{(2)}}. \tag{16}$$

The fractions of $\mathrm{Zn}^{(i)}$ species estimated by using Eqs.(15) and (16) show that the proportions of $\mathrm{Zn}^{(1)}$ and $\mathrm{Zn}^{(2)}$ increase with temperature as the proportion of $\mathrm{Zn}^{(0)}$ decreases (Fig. 9(d)). For liquid $\mathrm{ZnCl_2}$ at 800 K, molecular dynamics simulations using a polarizable ion model find comparable fractions of $\mathrm{Zn}^{(0)}$, $\mathrm{Zn}^{(1)}$ and $\mathrm{Zn}^{(2)}$ species at 45, 36 and 19%, respectively [29].

5.2. Structure of glassy and liquid ZnCl₂ using the Bhatia-Thornton formalism

The Bhatia-Thornton partial structure factors $S_{IJ}^{\mathrm{BT}}(k)$ for the glass and for the liquid at different temperatures are shown in Fig. 13. All three of the functions have an FSDP at $\simeq 1$ Å^{-1} and a principal peak or trough at $\simeq 2.09$ Å^{-1}, where the height of the latter decreases with increasing temperature. The corresponding partial pair-distribution functions $g_{IJ}^{\mathrm{BT}}(r)$ all show common features that broaden with increasing temperature (Fig. 14). The trough in $g_{CC}^{\mathrm{BT}}(r)$ at $\simeq 2.28$ Å arises from unlike nearest-neighbors, and is therefore expected for a chemically ordered material.

An FSDP in $S_{CC}^{\mathrm{BT}}(k)$ has also been observed for several other network glass-forming materials with the MX₂ stoichiometry such as GeSe₂ [85–88]. The occurrence of this peak has proved controversial because it was not predicted from earlier classical molecular dynamics simulations or integral-equation calculations [89–92]. Additionally, in the scenario where these MX₂ materials can be regarded as purely ionic systems containing point-like cations and anions, $S_{CC}^{\mathrm{BT}}(k)$ is related to the charge-charge partial structure factor $S_{ZZ}(k)$ via the expression $S_{CC}^{\mathrm{BT}}(k) = c_{\mathrm{M}}c_{\mathrm{X}}S_{ZZ}(k)$. An FSDP in $S_{CC}^{\mathrm{BT}}(k)$ then implies a non-uniformity in the charge distribution on an intermediate length scale [49].

The issue of concentration versus charge fluctuations on an intermediate length scale in MX₂ materials was addressed by Massobrio and co-workers via first-principles molecular dynamics simulations [88, 94]. In this work $S_{CC}^{\mathrm{BT}}(k)$, which depends on the atomic positions, was calculated separately

from $S_{ZZ}(k)$, which depends on the valence-electron density. No evidence was found in any of the investigated systems for intermediate ranged charge fluctuations i.e. an FSDP for $S_{ZZ}(k)$ was not found. This led to a proposal for three classes of network-forming systems: Class I systems have perfect chemical order and no FSDP in $S_{CC}^{BT}(k)$; class II systems have a moderate number of defects in an otherwise chemically ordered network and an FSDP in $S_{CC}^{BT}(k)$; and class III systems have a large degree of chemical disorder, feature a rich variety of structural motifs, and show no FSDP in $S_{CC}^{BT}(k)$ [88].

The appearance of charge neutrality on an intermediate length scale provides an important constraint on the network connectivity that leads to these different network types. For example, in chemically ordered class I systems such as SiO_2 the network is made from the same type of charge-neutral motif and concentration fluctuations need not occur on an intermediate range. In comparison, in class II materials such as $GeSe_2$ and $SiSe_2$ there is a moderate number of chemical defects that can lead to M-centered structural motifs with different charges. These motifs must, however, assemble to form a network in which charge neutrality prevails on the length scale of a few structural motifs i.e. there is self-organization that leads to a non-uniform distribution of M-centered motifs such that concentration fluctuations occur on an intermediate range. In the case of class III systems, a large degree of chemical disorder leads to a break-down of the intermediate range order such that the FSDP becomes a less prominent feature in $S_N(k)$ or $S_X(k)$ and disappears from $S_{CC}^{BT}(k)$.[5]

Liquid and glassy $ZnCl_2$ are both chemically ordered and, according to the above, should therefore be categorized as class I network-forming materials. A small FSDP in $S_{CC}^{BT}(k)$ is, however, observed (Fig. 13). It is notable that for these disordered forms of $ZnCl_2$, edge-sharing tetrahedra are indicated by RMC models (Fig. 9(c)–(d)), by molecular dynamics simulations [29], and by Raman spectroscopy experiments [28]. It is also notable that in liquid $GeSe_2$ the FSDP in $S_{CC}^{BT}(k)$ has been attributed to edge-sharing motifs containing mis-coordinated atoms (i.e. those not satisfying the '8-N' rule) [84]; and in glassy $SiSe_2$, where there is also an FSDP in $S_{CC}^{BT}(k)$, the majority of Si atoms are involved in edge-sharing conformations [94, 95]. In

---

[5]$GeSe_2$ was originally classified as a class III system owing to the large structural disorder in the first-principles molecular dynamics model that was considered [88]. However, experimental results [85–87] and more recent first-principles molecular dynamics models [93] indicate it to be a class II material.

comparison, an FSDP in $S_{CC}^{\mathrm{BT}}(k)$ has not been found for glassy SiO_2 from diffraction experiments [96], but this peak has been found for glassy GeO_2 from both diffraction experiments [7, 14] and first-principles molecular dynamics simulations [97]. The networks for both of these materials are based on chemically ordered corner-sharing arrangements of MO_4 (M = Si or Ge) tetrahedra [4, 97]. The FSDP in $S_{CC}^{\mathrm{BT}}(k)$ for glassy GeO_2 does not appear to originate from coordination defects in the network structure since they were not present in the first-principles molecular dynamics model [97].

All of this evidence suggests a revised definition for class I and II network-forming systems, along the lines suggested in Ref. [31], such that class I systems form chemically ordered corner-sharing networks, while class II systems form networks that incorporate edge-sharing motifs and may include a moderate number of structural defects. An FSDP appears in $S_{CC}^{\mathrm{BT}}(k)$ for class II systems and originates primarily from edge-sharing motifs. A small FSDP may also appear in $S_{CC}^{\mathrm{BT}}(k)$ for class I systems but does not arise from the four-fold rings associated with these edge-sharing conformations. The concentration-concentration partial structure factor is thereby proving to be a sensitive probe of the ordering in network glass-forming materials.

6. Conclusions

A systematic investigation of the network glass-forming material $ZnCl_2$ was made by using a combination of neutron and high-energy x-ray diffraction over a wide temperature interval, ranging from the glass to the liquid close to its boiling point. The results show that the FSDP, which is a signature of intermediate range ordering, is a notable feature at all temperatures and is associated primarily with the Zn–Zn partial structure factor. The measured correlation lengths associated with the intermediate and extended range ordering have a reciprocal temperature dependence. The RMC models show temperature dependent structural variability in which three- and five-fold coordinated Zn atoms (denoted by Zn3 and Zn5, respectively) become more numerous as the temperature increases, along with the number of Zn atoms involved in either one or two edge-sharing conformations (denoted by $Zn^{(1)}$ and $Zn^{(2)}$, respectively). The observation of edge-sharing motifs is consistent with molecular dynamics simulations using a polarizable ion model in which these conformations are found to promote the fragility of tetrahedral glass-forming liquids [36]. The results suggest a modification of the classification scheme given by Massobrio *et al.* [88] for network-forming

MX$_2$ materials: Class I systems form chemically ordered corner-sharing networks; class II systems form networks that incorporate both corner- and edge-sharing motifs; and class III systems form networks that are chemically disordered. Class I and II networks may both exhibit an FSDP in $S_{CC}^{\mathrm{BT}}(k)$ where, in the case of class II materials, this feature originates primarily from edge-sharing conformations.

Acknowledgments

References

[1] S. R. Elliott, Physics of Amorphous Materials, 2nd ed. Longman, Harlow 1990.

[2] A. Feltz, Amorphous Inorganic Materials and Glasses, VCH, Weinheim, 1993.

[3] P. Boolchand (Ed.), Insulating and Semiconducting Glasses, Singapore, World Scientific, 2000.

[4] G. N. Greaves, S. Sen, Adv. Phys. 56 (2007) 1.

[5] P. S. Salmon, A. Zeidler, Phys. Chem. Chem. Phys. 15 (2013) 15286.

[6] P. S. Salmon, R. A. Martin, P. E. Mason, G. J. Cuello, Nature 435 (2005) 75.

[7] P. S. Salmon, A. C. Barnes, R. A. Martin, G. J. Cuello, Phys. Rev. Lett. 96 (2006) 235502.

[8] S. C. Moss, D. L. Price, in D. Adler, H. Fritzsche, S. R. Ovshinsky (Eds.) Physics of Disordered Materials, New York, Plenum, 1985, p 77.

[9] S. R. Elliott, Nature 354 (1991) 445.

[10] P. S. Salmon, Proc. R. Soc. Lond. A 445 (1994) 351.

[11] D. L. Price, S. C. Moss, R. Reijers, M.-L. Saboungi, S. Susman, J. Phys. C: Solid State Phys. 21 (1988) L1069.

[12] P. S. Salmon, J. Phys.: Condens. Matter 19 (2007) 455208.

[13] A. B. Bhatia, D. E. Thornton, Phys. Rev. B. 2 (1970) 3004.

[14] P. S. Salmon, A. C. Barnes, R. A. Martin, G. J. Cuello, J. Phys.: Condens. Matter 19 (2007) 415110.

[15] C. A. Angell, Science 267 (1995) 1924.

[16] J. K. R. Weber, J. J. Felten, B. Cho, P. C. Nordine, Nature 393 (1998) 769.

[17] J. D. Mackenzie, W. K. Murphy, J. Chem. Phys. 33 (1960) 366.

[18] C. A. Angell, J. Wong, J. Chem. Phys. 53 (1970) 2053.

[19] S. Biggin, J. E. Enderby, J. Phys. C: Solid State Phys. 14 (1981) 3129.

[20] R. Triolo, A. H. Narten, J. Chem. Phys. 74 (1981) 703.

[21] J. A. E. Desa, A. C. Wright, J. Wong, R. N. Sinclair, J. Non-Cryst. Solids 51 (1982) 57.

[22] D. A. Allen, R. A. Howe, N. D. Wood, W. S. Howells, J. Chem. Phys. 94 (1991) 5071.

[23] M. Wilson and P. A. Madden, J. Phys.: Condens. Matter 5 (1993) 6833.

[24] E. A. Pavlatou, S. N. Yannopoulos, G. N. Papatheodorou, G. Fytas, J. Phys. Chem. B 101 (1997) 8748.

[25] J. Neuefeind, K. Tödheide, A. Lemke, H. Bertagnolli, J. Non-Cryst. Solids 224 (1998) 205.

[26] J. Neuefeind, Phys. Chem. Chem. Phys. 3 (2001) 3987.

[27] M. Wilson, P. A. Madden, Phys. Rev. Lett. 80 (1998) 532.

[28] S. N. Yannopoulos, A. G. Kalampounias, A. Chrissanthopoulos, G. N. Papatheodorou, J. Chem. Phys. 118 (2003) 3197.

[29] B. K. Sharma, M. Wilson, Phys. Rev. B 73 (2006) 060201(R).

[30] B. K. Sharma, M. Wilson, J. Phys.: Condens. Matter 20 (2008) 244123.

[31] M. Wilson, B. K. Sharma, J. Chem. Phys. 128 (2008) 214507.

[32] A. Zeidler, P. S. Salmon, R. A. Martin, T. Usuki, P. E. Mason, G. J. Cuello, S. Kohara, H. E. Fischer, Phys. Rev. B 82 (2010) 104208.

[33] A. Koura, S. Ohmura, F. Shimojo, J. Chem. Phys. 138 (2013) 134504.

[34] A. S. Özen, Z. Akdeniz, R. Ruberto, G. Pastore, M. P. Tosi, Phys. Lett. A 378 (2014) 431.

[35] D. R. Lide (Ed.), Handbook of Chemistry and Physics, 85th ed. Boca Raton, CRC Press, 2004.

[36] M. Wilson, P. S. Salmon, Phys. Rev. Lett. 103 (2009) 157801.

[37] M. Wilson, Phys. Chem. Chem. Phys. 14 (2012) 12701.

[38] R. Böhmer, K. L. Ngai, C. A. Angell, D. J. Plazek, J. Chem. Phys. 99 (1993) 4201.

[39] J. C. Wasse, P. S. Salmon, J. Phys.: Condens. Matter 10 (1998) 8139.

[40] A. Cavagna, Phys. Rep. 476 (2009) 51.

[41] W. Kob, J. Phys.: Condens. Matter 11 (1999) R85.

[42] J. C. Dyre, Rev. Mod. Phys. 78 (2006) 953.

[43] P. A. Madden, M. Wilson, Chem. Soc. Rev. 25 (1996) 339.

[44] P. S. Salmon, J. Phys.: Condens. Matter 17 (2005) S3537.

[45] P. S. Salmon, J. Phys.: Condens. Matter 18 (2006) 11443.

[46] R. L. McGreevy, J. Phys.: Condens. Matter 13 (2001) R877.

[47] H. E. Fischer, A. C. Barnes, P. S. Salmon, Rep. Prog. Phys 69 (2006) 233.

[48] T. E. Faber, J. M. Ziman, Phil. Mag. 11 (1965) 153.

[49] P. S. Salmon, Proc. R. Soc. Lond. A 437 (1992) 591.

[50] V. F. Sears, Neutron News 3(3) (1992) 26.

[51] C. A. Angell, E. Williams, K. J. Rao, J. C. Tucker, J. Phys. Chem. 81 (1977) 238.

[52] C. A. Angell, in: K. L. Ngai, G. B. Wright (Eds.) Relaxations in Complex Systems, Washington DC, Naval Research Laboratory, 1985, p. 3.

[53] E. Kartini, M. F. Collins, F. Mezei, E. C. Svensson, Physica B 241–243 (1998) 909.

[54] H. E. Fischer, G. J. Cuello, P. Palleau, D. Feltin, A. C. Barnes, Y. S. Badyal, J. M. Simonson, Appl. Phys. A 74 (2002) S160.

[55] H. Bertagnolli, P. Chieux, M. D. Zeidler, Mol. Phys. 32 (1976) 759.

[56] J. F. Jal, C. Mathieu, P. Chieux, and J. Dupuy, Phil. Mag. B 62 (1990) 351.

[57] J. O'M. Bockris, A. Pilla, J. L. Barton, Rev. Chim. Acad. Repub. Pop. Roum. 2 (1962) 59.

[58] S. Kohara, M. Itou, K. Suzuya, Y. Inamura, Y. Sakurai, Y. Ohishi, M. Takata, J. Phys.: Condens. Matter 19 (2007) 506101.

[59] E. N. Maslen, A. G. Fox, M. A. O'Keefe, in: A. J. C. Wilson, E. Prince (Eds.) International Tables for Crystallography vol C, 2nd ed., Dordrecht, Kluwer, 1999, section 6.1.1, p. 548.

[60] D. T. Cromer, J. B. Mann, J. Chem. Phys. 47 (1967) 1892.

[61] D. T. Cromer, J. Chem. Phys. 50 (1969) 4857.

[62] G. J. Janz, R. P. T. Tomkins, C. B. Allen, J. R. Downey Jr., G. L. Gardner, U. Krebs, S. K. Singer, J. Phys. Chem. Ref. Data 4 (1975) 871.

[63] P. S. Salmon, J. Phys. F: Met. Phys. 18 (1988) 2345.

[64] P. S. Salmon, S. Xin, H. E. Fischer, Phys. Rev. B 58 (1998) 6115.

[65] B. van Laar, W. B. Yelon, J. Appl. Cryst. 17 (1984) 47.

[66] L. W. Finger, D. E. Cox, A. P. Jephcoat, J. Appl. Cryst. 27 (1994) 892.

[67] P. S. Salmon, I. Petri, P. H. K. de Jong, P. Verkerk, H. E. Fischer, W. S. Howells, J. Phys.: Condens. Matter 16 (2004) 195.

[68] W. S. Howells, Nucl. Instrum. Methods Phys. Res. 219 (1984) 543.

[69] O. Gereben, P. Jóvári, L. Temleitner, L. Pusztai, J. Optoelectron. Adv. Mater. 9 (2007) 3021.

[70] A. Zeidler, J. W. E. Drewitt, P. S. Salmon, A. C. Barnes, W. A. Crichton, S. Klotz, H. E. Fischer, C. J. Benmore, S. Ramos, A. C. Hannon, J. Phys.: Condens. Matter 21 (2009) 474217.

[71] M. Kaupp, H. G. von Schnering, Inorg. Chem. 33 (1994) 4718.

[72] S. Le Roux, V. Petkov, J. Appl. Crystallogr. 43 (2010) 181.

[73] B. Brehler, Naturwissenschaft. 46 (1959) 554.

[74] B. Brehler, Z. Kristallogr. 115 (1961) 373.

[75] H. L. Yakel, J. Brynestad, Inorg. Chem. 17 (1978) 3294.

[76] M. G. Tucker, D. A. Keen, J. S. O. Evans, M. T. Dove, J. Phys.: Condens. Matter 19 (2007) 335215.

[77] M. Hargittai, J. Tremmel, I. Hargittai, Inorg. Chem. 25 (1986) 3163.

[78] M. Hargittai, Struct. Chem. 16 (2005) 33.

[79] K. J. Donald, M. Hargittai, R. Hoffmann, Chem. Eur. J. 15 (2009) 158.

[80] G. D. Scott, D. M. Kilgour, J. Phys. D: Appl. Phys. 2 (1969) 863.

[81] S. Le Roux, P. Jund, Comput. Mater. Sci. 49 (2010) 70.

[82] S. Le Roux, P. Jund, Comput. Mater. Sci. 50 (2011) 1217.

[83] S. V. King, Nature 213 (1967) 1112.

[84] C. Massobrio, A. Pasquarello, Phys. Rev. B 75 (2007) 014206.

[85] I. T. Penfold, P. S. Salmon. Phys. Rev. Lett. 67 (1991) 97.

[86] I. Petri, P. S. Salmon, H. E. Fischer, Phys. Rev. Lett. 84 (2000) 2413.

[87] P. S. Salmon, I. Petri, J. Phys.: Condens. Matter 15 (2003) S1509.

[88] C. Massobrio, M. Celino, A. Pasquarello, Phys. Rev. B 70 (2004) 174202.

[89] P. Vashishta, R. K. Kalia, G. A. Antonio, I. Ebbsjö, Phys. Rev. Lett. 62 (1989) 1651.

[90] P. Vashishta, R. K. Kalia, I. Ebbsjö, Phys. Rev. B 39 (1989) 6034.

[91] H. Iyetomi, P. Vashishta, R. K. Kalia, Phys. Rev. B 43 (1991) 1726.

[92] P. Vashishta, R. K. Kalia, J. P. Rino, I. Ebbsjö, Phys. Rev. B 41 (1990) 12197.

[93] A. Bouzid, C. Massobrio, J. Chem. Phys. 137 (2012) 046101.

[94] C. Massobrio, Lect. Notes Phys. 795 (2010) 343.

[95] M. Celino, C. Massobrio, Phys. Rev. Lett. 90 (2003) 125502.

[96] Q. Mei, C. J. Benmore, S. Sen, R. Sharma, J. L. Yarger, Phys. Rev. B. 78 (2008) 144204.

[97] L. Giacomazzi, P. Umari, A. Pasquarello, Phys. Rev. B 74 (2006) 155208.
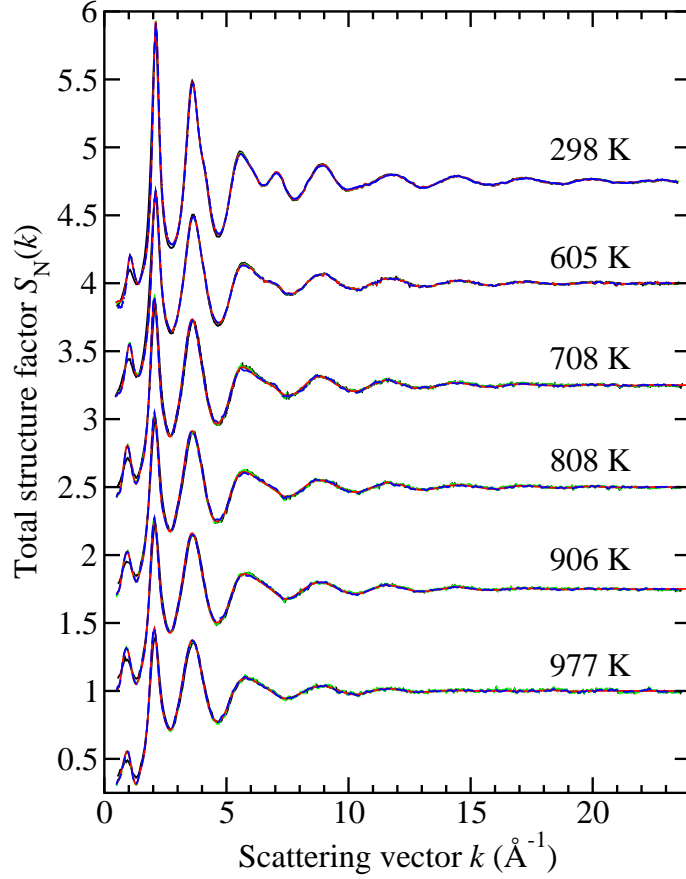
Figure 1: The neutron total structure factor $S_N(k)$ for glassy and liquid $ZnCl_2$ where the results for the glass at 298 K and for the liquid at 605 K are taken from Ref. [32]. The vertical bars represent the measured data points with statistical errors after the resolution function correction, and are indistinguishable at most k-values from the solid light (red) curves which give the back Fourier transforms of the corresponding $G_N(r)$ functions shown in Fig. 5 by the solid dark (black) curves. The broken (blue) curves correspond to the RMC models from the present work, and the discrepancy between the measured and modeled data sets is smaller than the line thickness at most k-values. The solid (black) curves give the measured functions before the resolution function correction and are distinguishable from the other curves at small k-values. Several of the data sets have been displaced vertically for clarity of presentation.
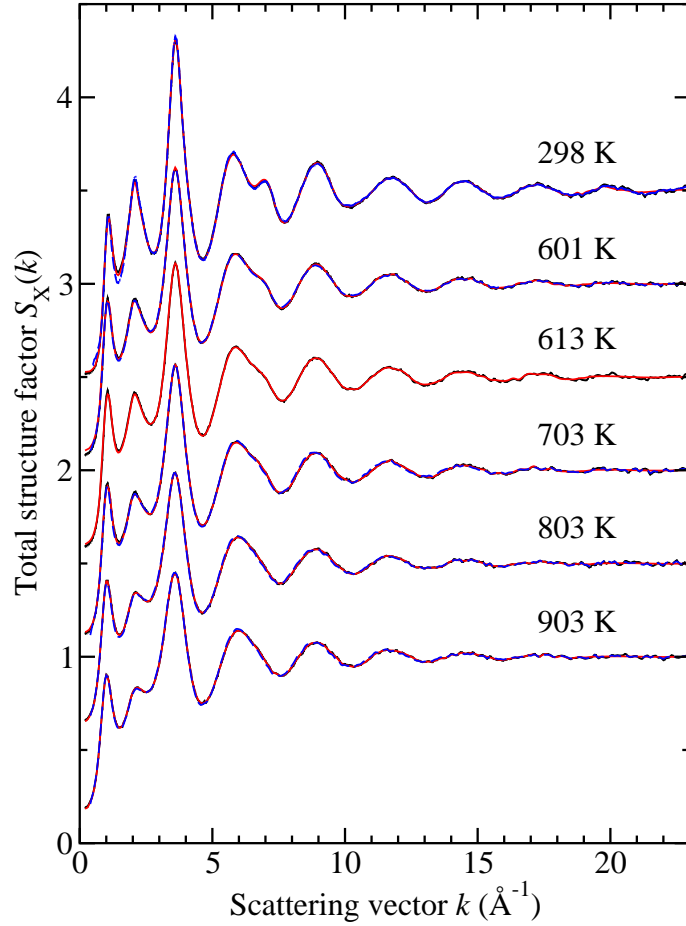
Figure 2: The x-ray total structure factor $S_X(k)$ for glassy and liquid $ZnCl_2$. The solid dark (black) curves give the measured functions and the solid light (red) curves give the back Fourier transforms of the $G_X(r)$ functions shown by the solid dark (black) curves in Fig. 6. The broken (blue) curves correspond to the RMC models from the present work, and the discrepancy between the measured and modeled data sets is smaller than the line thickness at most k-values. Several of the curves have been displaced vertically for clarity of presentation.
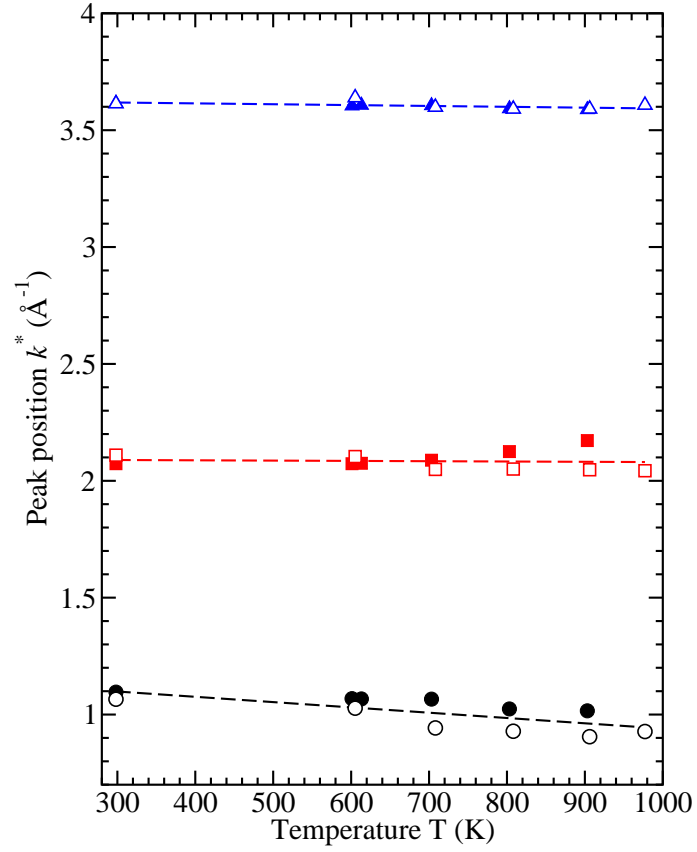
Figure 3: The temperature dependence of the position k^* of the FSDP (circles), principal peak (squares) and third peak (triangles) in the measured $S_N(k)$ (open symbols) and $S_X(k)$ (closed symbols) functions for glassy and liquid $ZnCl_2$. The neutron diffraction results correspond to resolution-function corrected data sets. The symbol sizes are comparable to the magnitude of the statistical errors, and the straight line fits are drawn as guides for the eye.
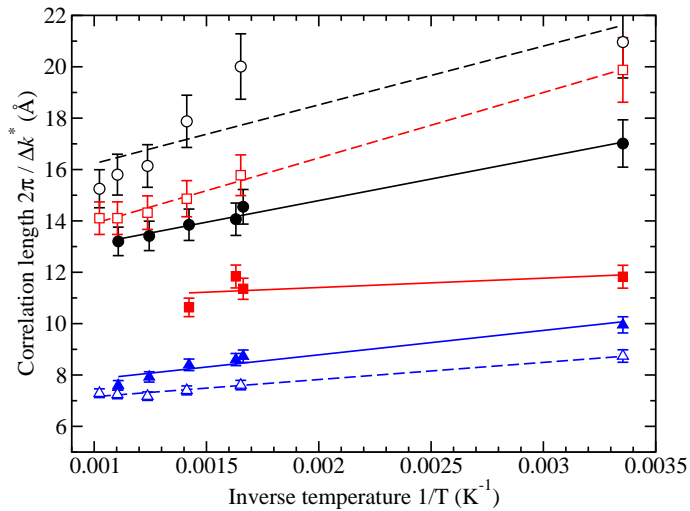
Figure 4: The inverse temperature dependence of the real-space correlation lengths $2\pi/\Delta k^*$ as obtained from the FSDP (circles), principal peak (squares) and third peak (triangles) in the measured $S_N(k)$ (open symbols) and $S_X(k)$ (closed symbols) functions for glassy and liquid $ZnCl_2$. The neutron diffraction results correspond to resolution-function corrected data sets. Each full-width at half-maximum Δk^* was measured relative to a baseline drawn between the minima on either side of a peak maximum. This procedure does not lead to finite widths for the principal peak in $S_X(k)$ at the highest temperatures, so the corresponding data points are omitted. The straight line fits are drawn as guides for the eye.
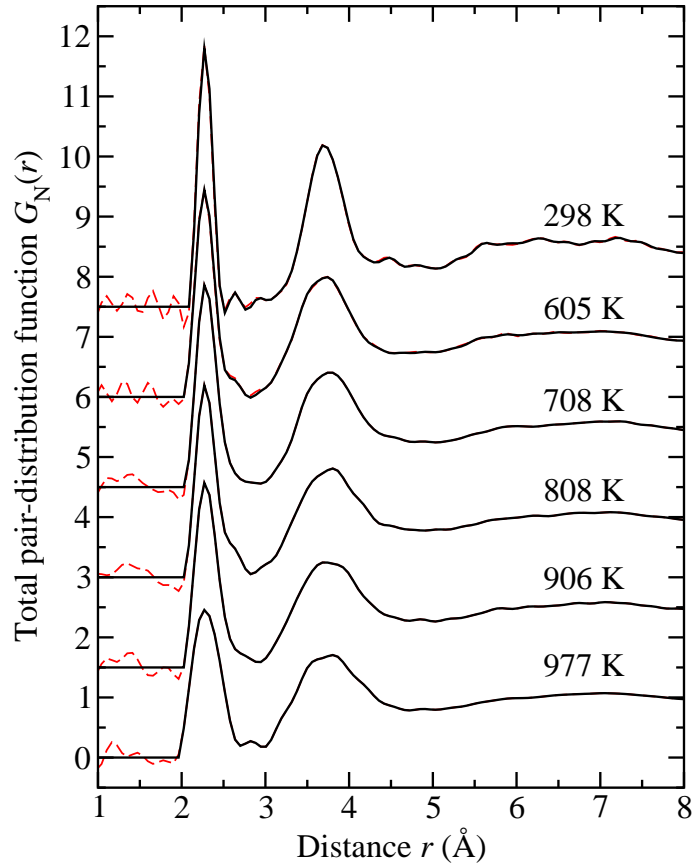
Figure 5: The neutron total pair-distribution function $G_N(r)$ for glassy and liquid $ZnCl_2$. The solid dark (black) curves were obtained by Fourier transforming the measured resolution-function corrected $S_N(k)$ functions given in Fig. 1 after spline fitting, and the broken (red) curves show the extent of the unphysical small-r oscillations. Several of the curves have been displaced vertically for clarity of presentation.
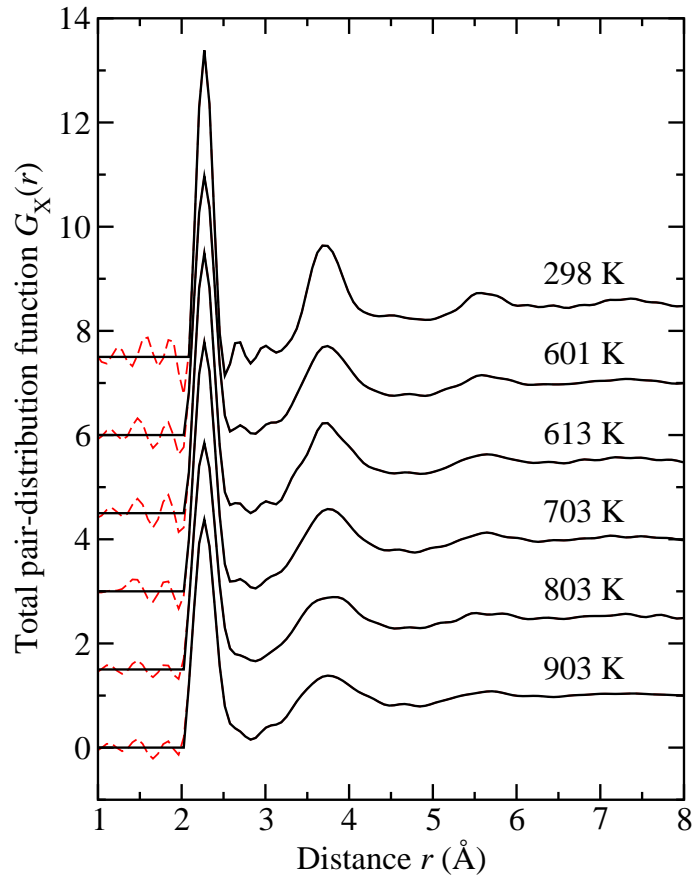
Figure 6: The x-ray total pair-distribution function $G_X(r)$ for glassy and liquid ZnCl$_2$. The solid dark (black) curves were obtained by Fourier transforming the measured $S_X(k)$ functions given in Fig. 2 after spline fitting and applying a cosine window function to the last few data points, and the broken (red) curves show the extent of the unphysical small-r oscillations. Several of the curves have been displaced vertically for clarity of presentation.
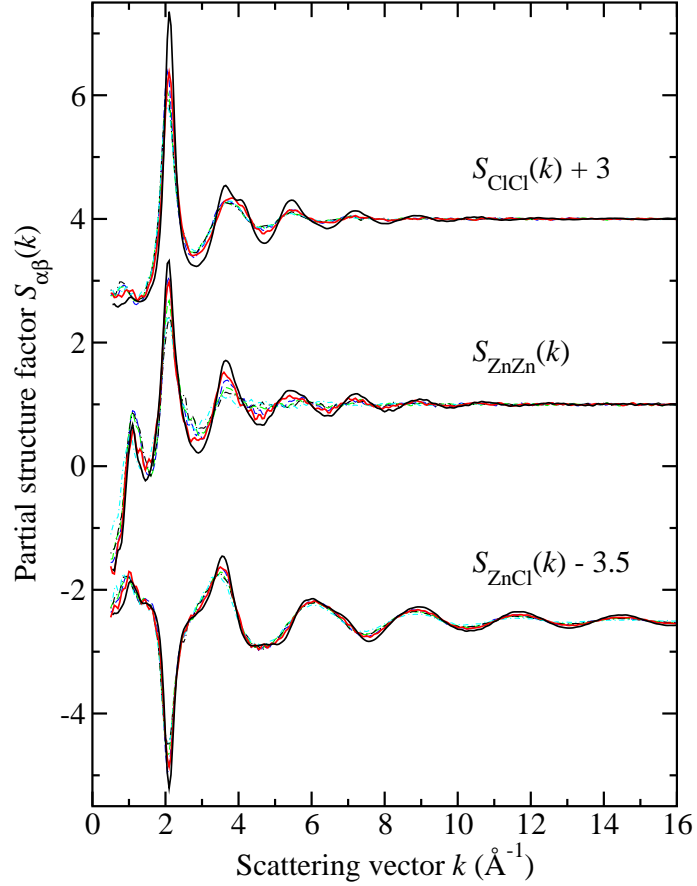
Figure 7: The Faber-Ziman partial structure factors $S_{\alpha\beta}(k)$ from RMC models of glassy and liquid $ZnCl_2$ obtained in the present work. Models for the glass [solid dark (black) curves] and for the liquid at average temperatures of 603(5) K [solid light (red) curves], 706(3) K [broken dark (blue) curves], 806(3) K [broken light (green) curves] and 905(2) K [chained dark (black) curves] were generated from the x-ray diffraction and resolution-function corrected neutron diffraction data shown in Figs. 1 and 2. The model for the liquid at 977(2) K [chained light (cyan) curves] was generated from the resolution-function corrected neutron diffraction data shown in Fig. 1.
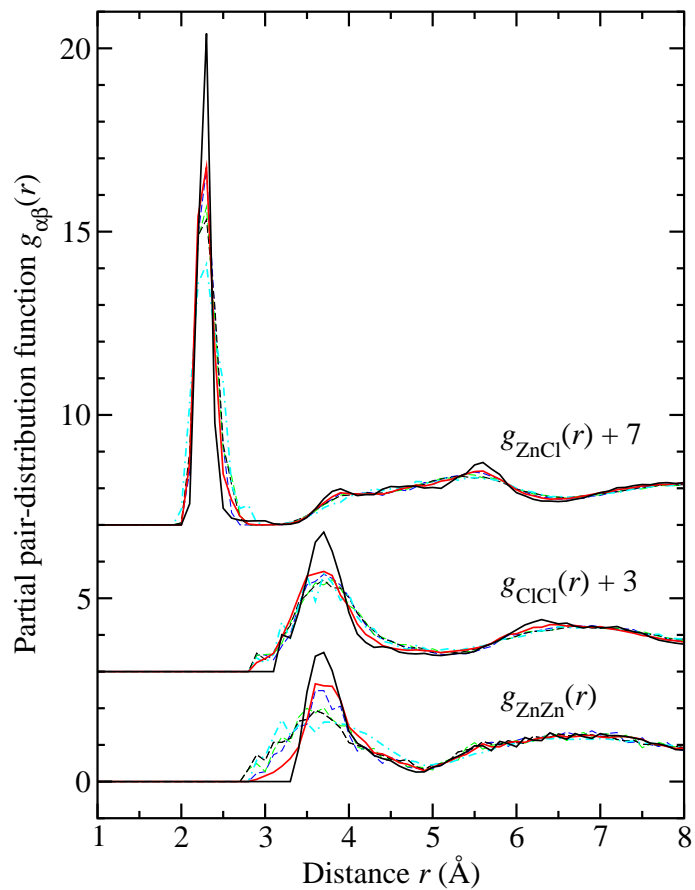
Figure 8: The partial pair-distribution functions $g_{\alpha\beta}(r)$ from RMC models of glassy and liquid $ZnCl_2$ obtained in the present work. The identity of the curves is described in the Fig. 7 legend.
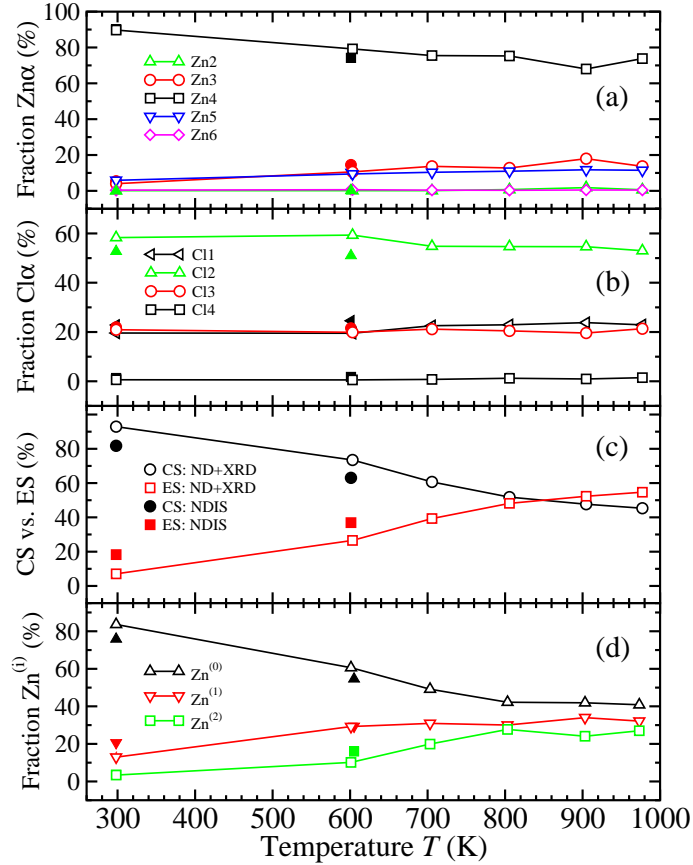
Figure 9: The temperature dependence of (a) the fractions of $Zn\alpha$ ($\alpha = 2, 3, 4, 5$ or 6) species; (b) the fractions of $Cl\alpha$ ($\alpha = 1, 2, 3$ or 4) species; (c) the fractions of corner-sharing (CS) and edge-sharing (ES) Zn4-centered tetrahedra; and (d) the fractions of $Zn^{(i)}$ ($i = 0, 1, 2$) atoms. The open symbols show the results obtained from the RMC models of the present work for glassy and liquid $ZnCl_2$. The closed symbols show the results obtained from the NDIS-based RMC models of Ref. [32] for the glass and for the liquid at 605 K. The open symbols often superpose the closed symbols.
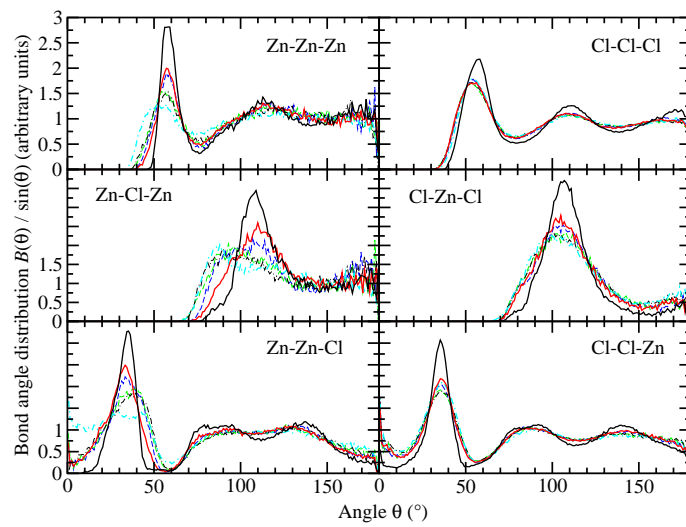
Figure 10: The bond angle distributions for the RMC models of glassy and liquid ZnCl$_2$ obtained in the present work. The identity of the curves is described in the Fig. 7 legend.
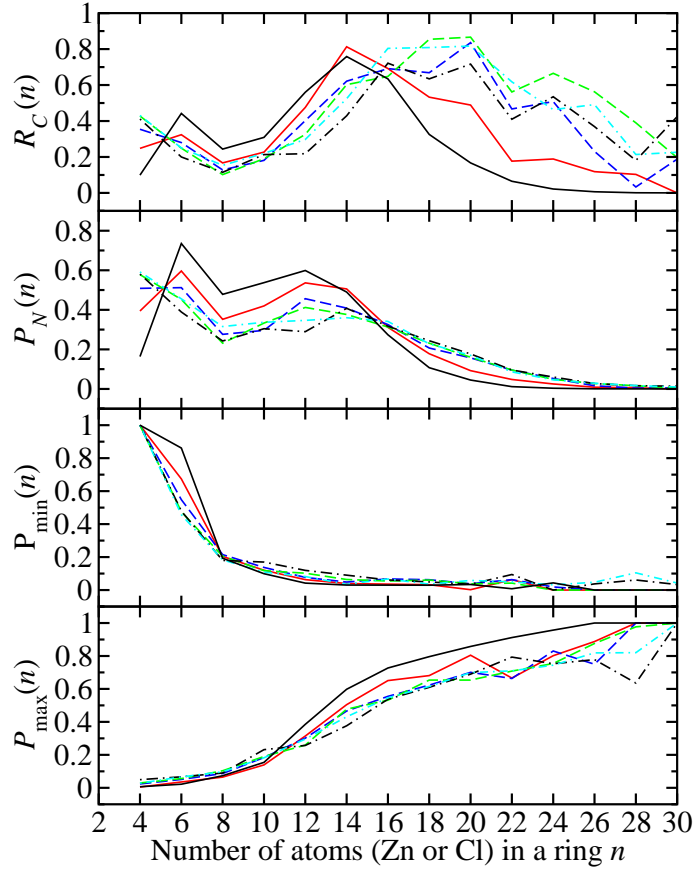
Figure 11: The connectivity profiles for the RMC models of glassy and liquid $ZnCl_2$ obtained in the present work where Zn atoms were used to initiate shortest path searches. $R_C(n)$ is proportional to the number of rings containing n atoms (Zn or Cl); $P_N(n)$ is proportional to the number of Zn atoms that can be used as a starting point to initiate a search for at least one ring containing n atoms; and for a given Zn atom in an n-fold ring, $P_{\min}(n)$ (or $P_{\max}(n)$) gives the probability that this ring constitutes the shortest (or longest) closed path that can be found by using this Zn atom to initiate a search. No odd-membered rings were found i.e. the networks are chemically ordered. The identity of the curves is described in the Fig. 7 legend.
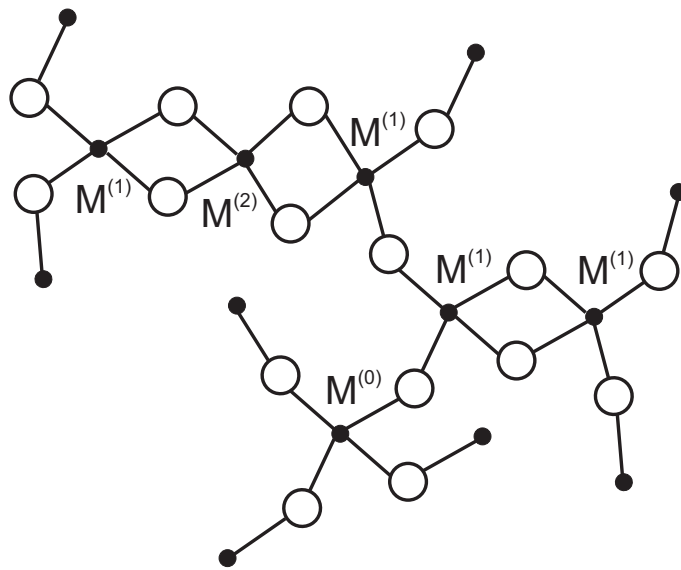
35

Figure 12: A schematic for an MX_2 material in which M atoms (closed circles) are distinguished according to whether they are involved in one four-fold ring $M^{(1)}$, two four-fold rings $M^{(2)}$, or no four-fold rings $M^{(0)}$. An 'isolated' four-fold ring containing two $M^{(1)}$ atoms is shown to the right hand side. The X atoms are represented by open circles.
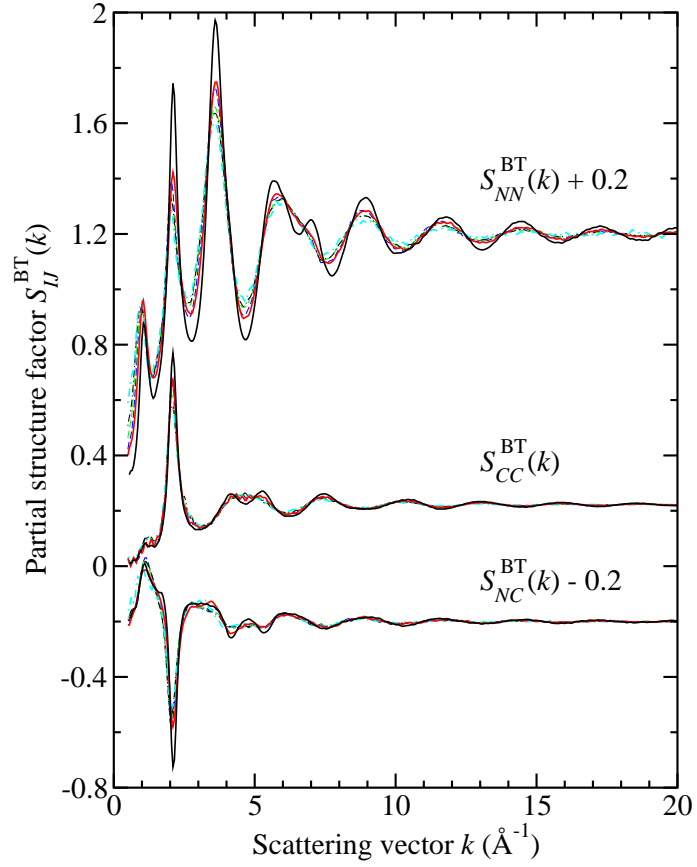
Figure 13: The Bhatia-Thornton partial structure factors $S_{IJ}^{\mathrm{BT}}(k)$ from the RMC models of glassy and liquid $ZnCl_2$ obtained in the present work. The identity of the curves is described in the Fig. 7 legend.
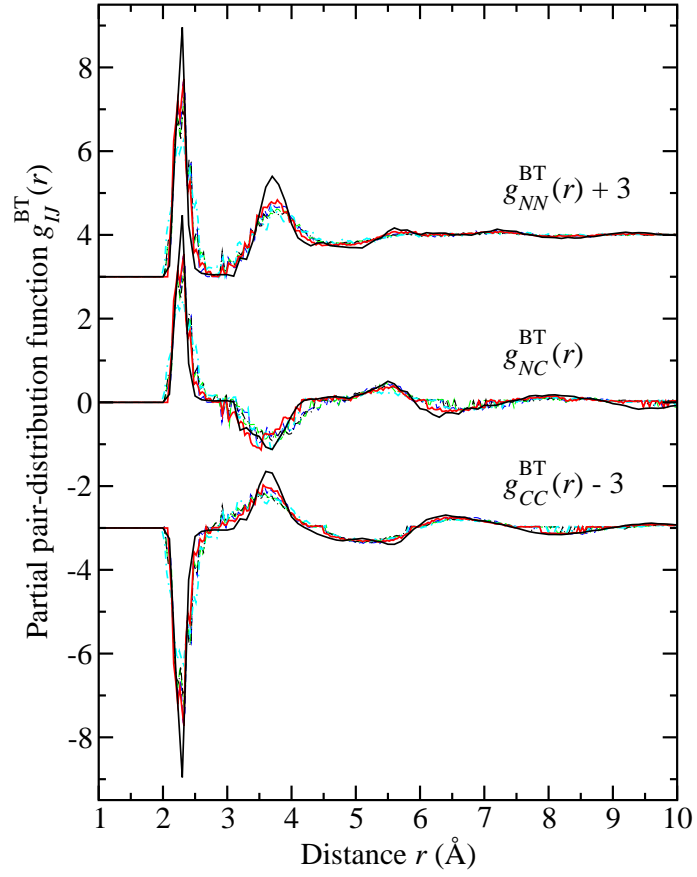
Figure 14: The Bhatia-Thornton partial pair-distribution functions $g_{IJ}^{\mathrm{BT}}(r)$ from the RMC models of glassy and liquid $ZnCl_2$ obtained in the present work. The identity of the curves is described in the Fig. 7 legend.